Remote Entanglement Generation Via Enhanced Quantum State Transfer

Tian-Le Wang,[1,2] Peng Wang,[1,2,3] Ze-An Zhao,[1,2] Sheng Zhang,[1,2,3] Ren-Ze Zhao,[1,2] Xiao-Yan Yang,[1,2] Hai-Feng Zhang,[1,2] Zhi-Fei Li,[1,2] Yuan Wu,[1,2] Liang-Liang Guo,[4] Yong Chen,[4] Hao-Ran Tao,[4] Lei Du,[4] Chi Zhang,[4] Zhi-Long Jia,[4] Wei-Cheng Kong,[4] Peng Duan,[1,2,*] Ming Gong,[1,2,5,6,†] and Guo-Ping Guo[1,2,4,‡]

[1] *Laboratory of Quantum Information, University of Science and Technology of China, Hefei 230026, China*

[2] *Synergetic Innovation Center of Quantum Information and Quantum Physics, University of Science and Technology of China, Hefei 230026, China*

[3] *Suzhou Institute for Advanced Research, University of Science and Technology of China, Suzhou, Jiangsu 215123, China*

[4] *Origin Quantum, Hefei, Anhui 230088, China*

[5] *Hefei National Laboratory, University of Science and Technology of China, Hefei 230088, China*

[6] *Anhui Province Key Laboratory of Quantum Network, University of Science and Technology of China, Hefei 230026, China*

(Received 29 September 2025; accepted 4 February 2026; published 10 March 2026)

Achieving robust and scalable remote quantum entanglement is one of the fundamental challenges for the development of distributed quantum networks and modular quantum computing systems. In this context, perfect state transfer (PST) and fractional state transfer (FST) have emerged as promising schemes for quantum state transfer and remote entanglement generation using only nearest-neighbor couplings. In this work, we propose a quantum state transfer scheme based on a zig-zag configuration, which introduces a control parameter for PST and FST. We show that this new parameter can suppress the population in the intermediate qubits, thereby reducing losses and enhancing state transfer. In certain limiting cases, our new scheme reduces to the conventional PST scheme, revealing an elegant mathematical structure inherent in the design. We experimentally demonstrate our proposed scheme on a superconducting quantum processor, achieving an 18% reduction in error for remote Bell state generation in a 1D (1×5) qubit chain with enhanced robustness to specific noise channels. Furthermore, we extend our approach to a 2D (3×3) network and successfully generate a $\mathcal{W}$ state among the four corner qubits. These results highlight the potential of our new enhanced quantum state transfer scheme for scalable and noise-resilient quantum communication and computing.

DOI: 10.1103/4x8d-cmyx

I. INTRODUCTION

Quantum computing and quantum simulation have entered the noisy intermediate-scale quantum era [1,2]. Currently, quantum processors based on superconducting circuits [3–22], photons [23,24], trapped ions [25], neutral atoms [26], and other platforms have integrated hundreds of qubits on a single chip, with several teams publishing roadmaps to realize chips with thousands of qubits in the coming years. Among these, superconducting quantum chips are advancing rapidly due to their ease of fabrication and scalability. However, the static nature of their qubits restricts interactions to short ranges, hindering the efficient connectivity between distant qubits on the chip [27–38]. In this context, quantum state transfer and remote entanglement generation are essential for establishing remote qubit interconnections and ultimately enabling distributed quantum computing architectures [39].

Perfect state transfer (PST), in which an arbitrary state can be perfectly transferred from the leftmost site to the rightmost site, can be realized in a quantum circuit with only nearest-neighbor (NN) interactions in a pre-engineered Hamiltonian [40–42]. Furthermore,

*Contact author: pengduan@ustc.edu.cn
†Contact author: gongm@ustc.edu.cn
‡Contact author: gpguo@ustc.edu.cn

Published by the American Physical Society under the terms of the Creative Commons Attribution 4.0 International license. Further distribution of this work must maintain attribution to the author(s) and the published article's title, journal citation, and DOI.

fractional state transfer (FST), which can be regarded as an isospectral deformation of the PST Hamiltonian, enables the generation of remote entangled states between two distant sites [43]. With these ideas, the PST has been realized on various quantum hardware platforms [44–52]. Here, it is necessary to emphasize that the mechanisms of PST and FST differ fundamentally from those based on adiabatic passage or flying photons, which require precise control of pulse shapes [36,53–59].

In this work, we propose a new quantum state transfer scheme based on a zig-zag configuration, which can be reduced to the conventional PST scheme (referred to as the line configuration) in certain limiting cases, while offering much broader applicability. We show that our scheme, with a controllable parameter $m \in \mathbb{Z}^+$ between the adjacent sites, can suppress the state population in the intermediate qubits, thereby reducing the influence of decoherence during the state transfer process and enhancing remote entanglement generation between distant sites. In particular, in the two limits when $m = 0$ and $m \to \infty$, our scheme reduces to the conventional PST scheme by Christandl *et al.* [40], revealing some elegant mathematical structure hidden in our design. With this scheme and using a 1D qubit chain, we achieve an 18% reduction in error for remote Bell state generation compared to the traditional line configuration. Furthermore, we extend the application to a 2D (3×3) qubit network and successfully generate a $\mathcal{W}$ state among the four corner qubits, thus showcasing the scalability of our scheme. These results mark a significant step toward realizing the full potential of quantum state transfer and remote entanglement generation in next-generation quantum computing chips [3,5,10,14,17].

II. THE ZIG-ZAG CONFIGURATION: STRUCTURE AND SPECTRAL PROPERTIES

We start from the following Hamiltonian with NN *XY*-type interaction (with $\hbar = 1$):

$$H = \sum_{n=1}^{N} \frac{\omega_n}{2}\sigma_n^z + \sum_{n=1}^{N-1} J_n(\sigma_n^+\sigma_{n+1}^- + \sigma_n^-\sigma_{n+1}^+), \quad (1)$$

where $\sigma_n^{\pm,z}$ are the Pauli operators for qubit Q_n with frequency ω_n and J_n is the NN coupling between qubits Q_n and Q_{n+1}. In superconducting qubits, as used in this work, the coupling strength can be adjusted using a tunable coupler [60,61].

The goal of PST is to construct a Hamiltonian H_{PST} by engineering the qubit frequencies ω_n and coupling strengths J_n in Eq. (1), such that a quantum state initialized at the starting point $|1\rangle$ can be perfectly transferred to the end point $|N\rangle$ after a specific time τ. This can be expressed as $e^{-iH_{\mathrm{PST}}\cdot\tau}|1\rangle = e^{i\phi}|N\rangle$, where ϕ is a global phase that is independent of measurement. Here, we use the notation $|n\rangle$ to denote the single-excitation state where only the nth site is excited while all other sites remain in the ground state, that is, $|n\rangle = \sigma_n^+|\downarrow\downarrow\downarrow\cdots\downarrow\rangle$. Reference [42] provides necessary and sufficient conditions for achieving PST with the following three criteria:

$$\omega_n = \omega_{N+1-n}, \quad (2)$$

$$J_n^2 = J_{N-n}^2, \quad (3)$$

$$(\lambda_{n+1} - \lambda_n)\tau = (2m_n + 1)\pi, \quad m_n \in \mathbb{Z}^+, \quad (4)$$

where the eigenvalues λ_n are ordered in increasing value, i.e., $\lambda_n < \lambda_{n+1}$. Christandl *et al.* showed that perfect state transfer can be achieved when the coupling strengths J_n are mirror symmetric about the central lattice site and all qubit frequencies ω_n are resonant [40],

$$\omega_n = 0, \quad (5)$$

$$J_n = \frac{J}{2}\sqrt{n(N-n)}, \quad (6)$$

where J denotes the evolution frequency of the system. These conditions satisfy Eqs. (2)–(4), yielding PST. The corresponding Hamiltonian is related to the spin operator S_x in quantum mechanics, with equal energy-level spacing.

The configuration for PST in Eqs. (5) and (6), which we refer to as the line configuration, has been widely adopted in previous studies due to its simplicity and analytical elegance [44–46]. In this work, we focus on a generalized configuration that introduces an additional tunable parameter, which preserves the desirable properties of the line configuration while providing enhanced flexibility and robustness against noise. In our new configuration, eigenvalues are given by

$$\lambda_n(m)/J = \left\{-\frac{N-1}{2}, -\frac{N-1}{2}+1, \ldots, -1, 0, 2m+1, 2m+2, \ldots, 2m+\frac{N-1}{2}\right\}, \quad (7)$$

where N is odd and m is a non-negative integer, with an energy gap $\varepsilon_g = \lambda_{(N+3)/2} - \lambda_{(N+1)/2} = (2m+1)J$. Through the inverse eigenvalue process [62–64], we obtain

$$\omega_n(m) = \mu_{n+1}\cdot 2m\cdot J, \quad (8)$$

$$J_n(m) = \frac{J}{2}\sqrt{(n+\mu_n 2m)(N-n+\mu_{n+1}2m)}, \quad (9)$$

where $\mu_n = 1$ when n is odd and 0 when n is even. Clearly, Eqs. (8) and (9) satisfy the PST conditions in Eqs. (2)–(4). Due to the alternating frequencies of ω_n, we refer to it as the zig-zag configuration. The structures of the line and zig-zag configurations are illustrated in Figs. 1(a) and 1(b).

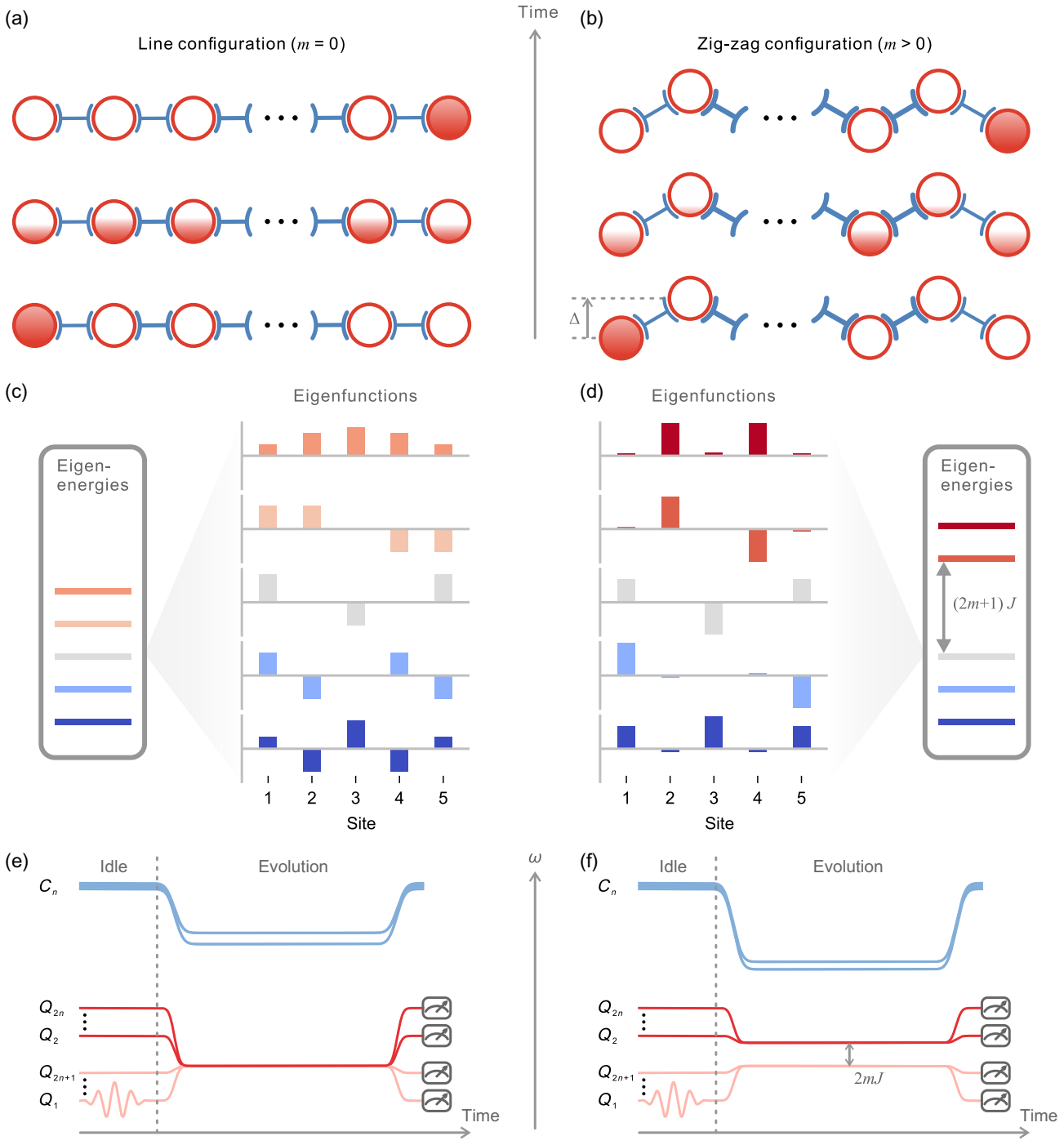


FIG. 1. Physical model. (a) and (b) Conceptual diagrams of the quantum state transfer. In the line configuration, all qubits have the same frequency, and the population is distributed across all qubits during the evolution. In the zig-zag configuration, the frequencies ω_n alternate between the odd and even qubits, leading to significant suppression of population on the even qubits during evolution. (c) and (d) Schematics of the eigenvalues and eigenfunctions, corresponding to the line configuration ($m = 0$) and zig-zag configuration ($m > 0$), respectively. For the line configuration, the eigenvalues have an equal energy-level spacing of 1. For the zig-zag configuration, there is an energy gap of $(2m + 1)J$ between states $|\lambda_{(N+1)/2}\rangle$ and $|\lambda_{(N+3)/2}\rangle$; see Eq. (7). Furthermore, the eigenfunctions are significantly suppressed on the even sites. The figure illustrates the case of $N = 5$ as an example. (e) and (f) Pulse sequences. At the initial time, all qubits and couplers are set to their idle points (i.e., no interactions between qubits and all couplers are turned off). A single-qubit gate X_π is applied to Q_1 to prepare a single-excitation state. Subsequently, all qubits and couplers are set to their target frequencies and coupling strengths via flattop Gaussian pulses to perform the desired dynamics. After the evolution, all qubits and couplers return to their idle points, followed by measurements on the qubits to read their states.

This configuration has two elegant limits that help us to understand its essential physics. First, when $m = 0$, this model is naturally reduced to the line configuration. Second, when $m \gg N/2$, the occupation of the even sites vanishes [65], yielding

$$\omega_n^{\text{eff}} = -\frac{J(N-1)}{4}, \tag{10}$$

$$J_n^{\text{eff}} = -\frac{J}{2}\sqrt{\frac{n+1}{2}\left(\frac{N+1}{2} - \frac{n+1}{2}\right)}, \tag{11}$$

where $n = 1, 3, 5, \ldots, N$. J_n^{eff} represents the effective coupling between the nth and $(n+2)$th sites. The detailed derivation is provided in Note 5 in the Supplemental Material [66]. In this limit, the model reduces to the line configuration consisting of approximately half of the sites, $(N+1)/2$, revealing an intrinsic and elegant mathematical structure underlying the Hamiltonian. Consequently, all configurations with different $m \in \mathbb{Z}^+$ can support PST and, under suitable conditions, enable the generation of remote entanglement. The construction of the zig-zag model using the inverse eigenvalue method, as well as its generalization to new physical models, will be reported elsewhere [64].

III. PERFECT STATE TRANSFER IN THE ZIG-ZAG CONFIGURATION

We select the 1×3, 1×5, and 3×3 regions on the Wukong quantum chip for experimental demonstration [67–71]. The detailed layout of this quantum chip and its corresponding parameters are presented in Notes 1 and 2 in the Supplemental Material [66]. We first validate the existence of PST in a 1×3 qubit chain, with the results shown in Fig. 2(a). To ensure that the coupling strengths J_1 and J_2 are tuned to the target values, we perform SWAP calibration experiments between Q_1–Q_2 and Q_2–Q_3 (with $J_1 = J_2$ due to mirror symmetry). We then fix ω_1 and ω_3, scan only ω_2 to vary the frequency detuning Δ ($\Delta = \omega_2 - \omega_{1,3}$, with $\omega_1 = \omega_3$ due to mirror symmetry) from -20 to 100 MHz. For each specific set of J_1, J_2, and Δ, we apply a single-qubit gate X_π at the initial time to prepare Q_1 in a single-excitation state. After 60 ns of evolution, we perform a single-shot readout on Q_3 to obtain its population, following the pulse sequences shown in Figs. 1(e) and 1(f). The experimental results in Fig. 2(a) show that the population reaches a maximum value (approximately unity) at the bright spots, indicating successful excitation transfer from Q_1 to Q_3, and thus confirming that the corresponding parameters constitute a PST solution. This model can be solved analytically for a 1×3 qubit chain, yielding the population of Q_3 at time τ,

$$P_{Q_3} = \frac{1}{4}\left(\cos\frac{\Omega\tau}{2} - \cos\frac{\Delta\tau}{2}\right)^2 + \frac{1}{4}\left(\frac{\Delta}{\Omega}\sin\frac{\Omega\tau}{2} - \sin\frac{\Delta\tau}{2}\right)^2, \tag{12}$$

where $\Omega^2 = \Delta^2 + 8J_{1,2}^2$. Clearly, PST is achieved when $P_{Q_3} = 1$, which occurs when the zig-zag conditions in Eqs. (8) and (9) are satisfied. The derivation and numerical results are presented in Note 6 in the Supplemental Material [66].

The first four bright spots from left to right in the first row correspond one-to-one to the analytical solutions from $m = 0$ to $m = 3$ given by Eqs. (8) and (9). Note that the first spot should, in principle, occur at exactly zero detuning. However, in this experiment, the frequency shift induced by the couplers was not compensated, resulting in the first spot occurring at detuning approximately 10 MHz [20,45]. From these experimental results, we extract the coupling strength corresponding to the first bright spot as $\tilde{J}_{1,2}(0)/2\pi \approx 6$ MHz. This value can also be obtained analytically via $J/2\pi = 1/2\tau = 8.3$ MHz, which yields $J_{1,2}(0)/2\pi = (\sqrt{2}/2)J/2\pi = 5.9$ MHz. Thus, the above two estimations are consistent with each other. Similarly, we calculate the values of $J_n(m)$ for $m = 1$, 2, and 3, yielding $J_{1,2}(1)/2\pi = 10.2$ MHz, $J_{1,2}(2)/2\pi = 13.2$ MHz and $J_{1,2}(3)/2\pi = 15.6$ MHz, all of which are in good agreement with the experimental results.

In Figs. 2(b) and 2(c), we perform a fine scan of the state transfer population as a function of detuning Δ and evolution time τ near the solutions for $m = 0$ and $m = 3$, respectively. When $m = 0$, population remains on the second site, and the system evolves under the three-qubit interaction, resulting in a fragmented pattern as shown in Fig. 2(b). However, when m becomes large, the second site is effectively integrated out, and the three-qubit interaction is reduced to an effective two-qubit model between Q_1 and Q_3, as described by Eqs. (10) and (11), leading to the continuous pattern shown in Fig. 2(c). In Figs. 2(d)–2(f), we further experimentally compare the performance of PST in a 1×5 qubit chain for different m. Before acquiring the experimental results, we perform the parameter calibration and optimization (see Notes 7 and 8 in the Supplemental Material for details [66]) to ensure that the actual parameters applied to the qubits and couplers are as close as possible to the theoretical values $\omega_n(m)$ and $J_n(m)$ given by Eqs. (8) and (9). It is worth noting that the qubit frequency compensation has already been incorporated during the qubit frequency calibration, as its goal is to tune each qubit to the target value $\omega_n(m)$ with all couplers turned on. After applying the optimized pulse parameters corresponding to different m values, we vary the pulse duration and perform simultaneous readout on all qubits to obtain the PST

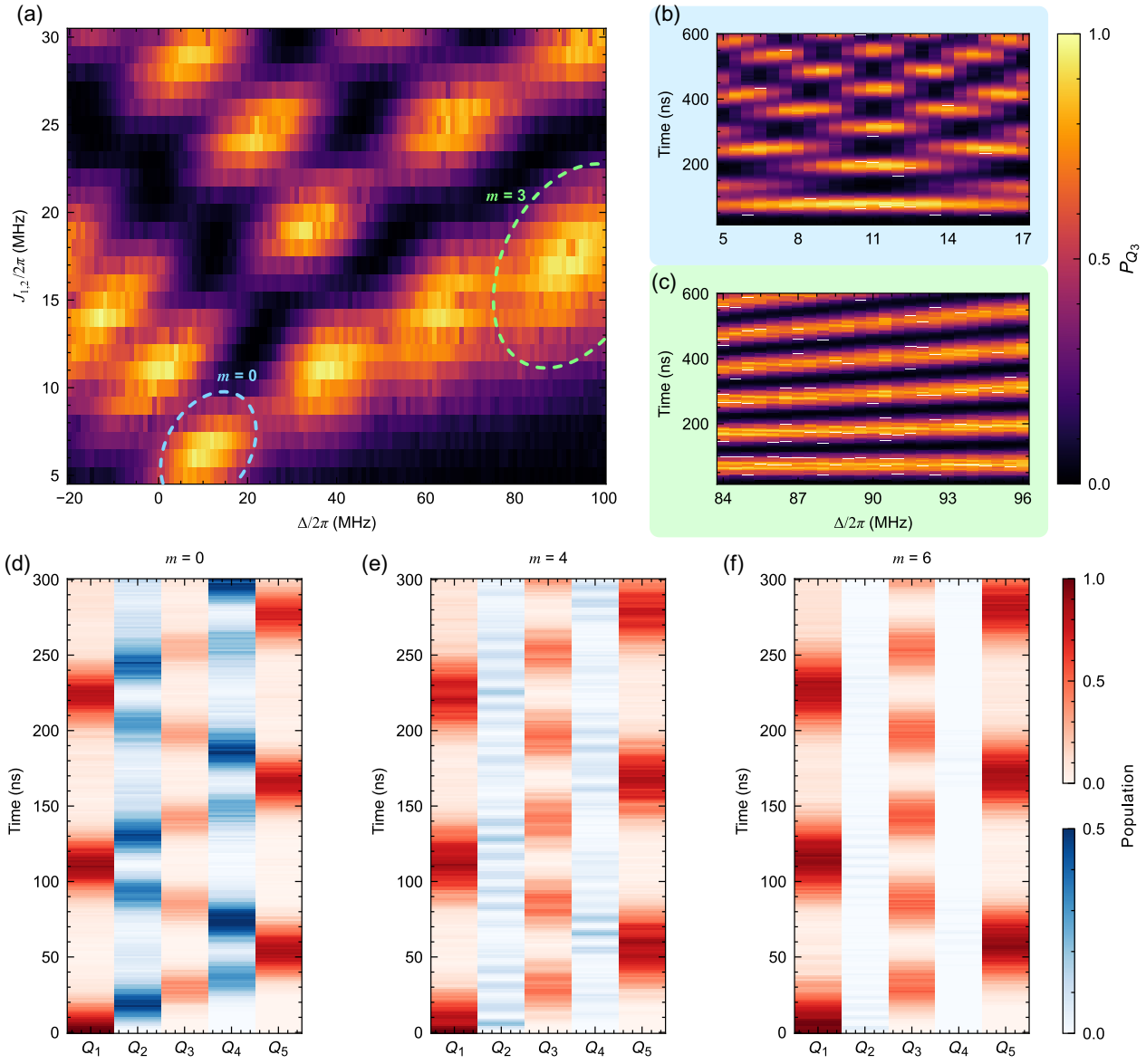


FIG. 2. Population evolution for perfect state transfer in 1D (1×3 and 1×5) qubit chains. (a) Population for a 1×3 chain as a function of $J_{1,2}$ and Δ ($\Delta = \omega_2 - \omega_{1,3}$). The colormap represents the population of qubit Q_3, measured after preparing an excitation on qubit Q_1 at the initial time and evolving for a fixed duration of $\tau = 60$ ns. Each bright spot represents a maximum population on Q_3, indicating the successful transfer of the excitation from Q_1 to Q_3. The corresponding evolution frequency is $J/2\pi = 1/2\tau = 8.3$ MHz. (b) and (c) Q_3 population evolution as a function of Δ, near the first (blue box) and fourth (green box) spots, respectively. (d)–(f) Perfect state transfer for $m = 0$, 4, 6 in a 1×5 qubit chain. One excitation is initialized on Q_1, and the population evolution of all qubits is measured simultaneously. For clarity, different scales and colormaps are used for the odd qubits (red, with a maximum of 1.0) and the even qubits (blue, with a maximum of 0.5). In these experiments, $J/2\pi$ is set to 9 MHz, corresponding to a target evolution time of $\tau = 55.6$ ns.

dynamics for $m = 0$, 4, and 6, respectively. As m increases, a noticeable reduction in the population of the even qubits is observed due to their being effectively integrated out in the effective Hamiltonian model as demonstrated by Eqs. (10) and (11). For $m = 6$, the residual population on the even qubits is below 0.05, compared with 0.54 when $m = 0$. The absence of these qubits during the dynamics indicates that their noise channels have been effectively shut off.

IV. REMOTE ENTANGLEMENT GENERATION VIA FRACTIONAL STATE TRANSFER

Based on the above observations, which validate our theoretical proposal, we next demonstrate remote entanglement generation using the zig-zag configuration and investigate the noise effects for various values of m. We follow the idea of FST, proposed by Genest *et al.* [43], i.e., $e^{-iH_{\mathrm{FST}}\cdot\tau}\,|1\rangle = e^{i\phi}(\sin 2\theta\,|1\rangle + \cos 2\theta\,|N\rangle)$. When $\theta =$

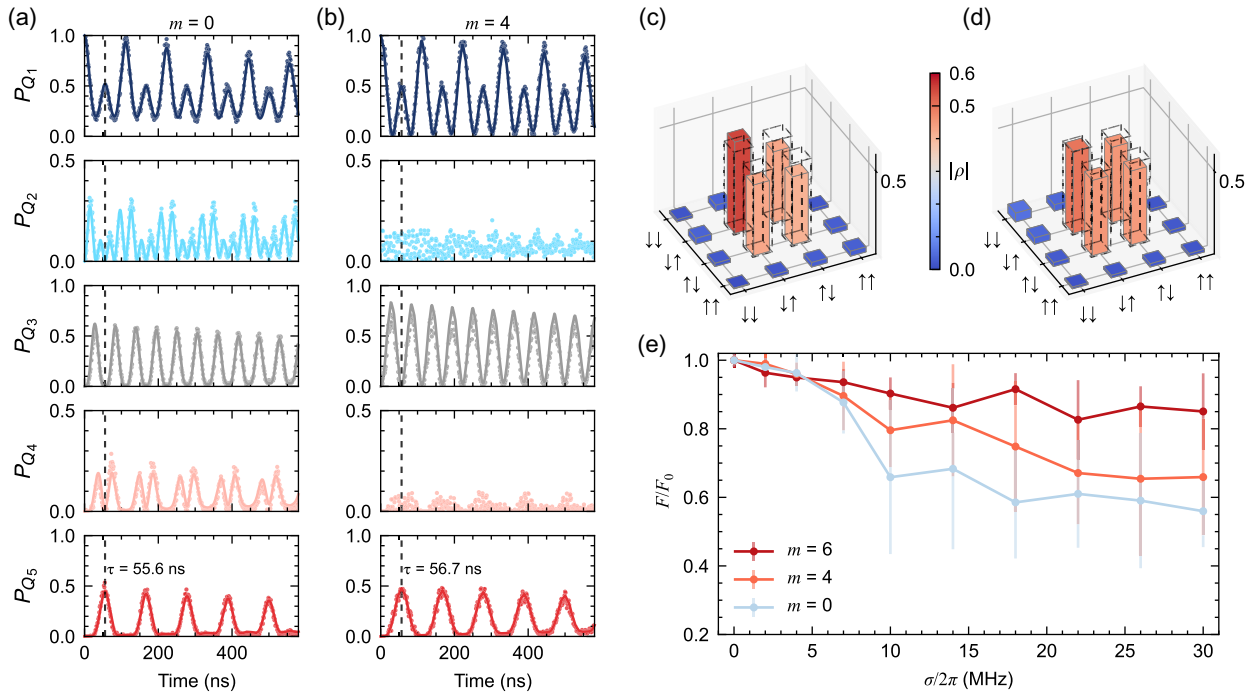


FIG. 3. Fractional state transfer and remote entanglement generation at various m in a 1D (1×5) qubit chain. (a) and (b) Fractional state transfer for $m = 0$ and $m = 4$, respectively. Initially, one excitation is prepared on Q_1, and at time t, the population of all qubits is measured simultaneously. The target evolution time is $\tau = 55.6$ ns, though deviations may occur in practice after the parameter optimization process. Symbols represent the experimental data, while the solid lines correspond to results from master equation simulations. (c) Quantum state tomography at τ=55.6 ns and $m = 0$. (d) The corresponding results at τ=56.7 ns and $m = 4$. The reconstructed density matrix yields the Bell state fidelity of 0.909 ± 0.024 and 0.925 ± 0.021 for these two conditions. The ideal Bell singlet state is $|\Psi^-\rangle = (|\downarrow\uparrow\rangle - |\uparrow\downarrow\rangle)/\sqrt{2}$, represented by the dashed box. The standard deviation of the fidelity is obtained from 50 experimental repetitions. (e) Fidelity degradation, F/F_0 (with F_0 being the fidelity at zero noise), as a function of frequency noise applied to the even qubits. The noise in the parameters follows a Gaussian distribution $N(0, \sigma)$, where σ is the noise intensity. Each data point represents the average of ten noise samples, with the error bars indicating the standard deviation of the fidelities.

$\pi/8$, the system evolves into a maximally entangled state between the remote sites $|1\rangle$ and $|N\rangle$. The PST model in Eqs. (8) and (9) cannot be directly used for this purpose and requires the following isospectral transformation [43]:

$$\tilde{J}_{\frac{N-1}{2}}(m) = (\cos\theta + \sin\theta) J_{\frac{N-1}{2}}(m),$$
$$\tilde{J}_{\frac{N+1}{2}}(m) = (\cos\theta - \sin\theta) J_{\frac{N+1}{2}}(m), \tag{13}$$

when N is odd, while all other frequencies and coupling terms remain the same as in Eqs. (8) and (9). A detailed discussion about FST is presented in Note 4 in the Supplemental Material [66].

Experimentally, we select $N = 5$ and $\theta = \pi/8$ and determine the Hamiltonian parameters $\omega_n(m)$ and $J_n(m)$ according to Eqs. (8), (9), and (13). Before obtaining the results shown in Figs. 3(a) and 3(b), we first calibrate each qubit frequency and coupling strength to their respective target values, $\omega_n(m)$ and $J_n(m)$, using single-qubit Ramsey and two-qubit SWAP experiments, respectively (see Note 7 in the Supplemental Material [66]). Based on these calibrated parameters, we then perform the FST experiments. Initially, a single-excitation state is prepared on Q_1 via a single-qubit gate X_π. Then the calibrated parameters are simultaneously applied to all qubits and couplers. After the parameter optimization procedure described in Note 8 in the Supplemental Material [66], the optimized FST dynamics are obtained, as shown in Figs. 3(a) and 3(b), corresponding to $m = 0$ and $m = 4$, respectively. For $m = 4$, the population of the even qubits is significantly suppressed compared to $m = 0$, leading to enhanced system coherence, as evidenced by the notably slower decay of the population envelope in Fig. 3(b) relative to Fig. 3(a). At $\tau = 55.6$ ns for $m = 0$ ($\tau = 56.7$ ns for $m = 4$), the population of the remote qubits, Q_1 and Q_5, approaches 0.5, while the population of the intermediate qubits is close to 0, suggesting that maximal entanglement has been achieved between Q_1 and Q_5. To further confirm the result, we perform the quantum state tomography [72] on Q_1 and Q_5 in Fig. 3(c), confirming that they are indeed the Bell singlet state $|\Psi^-\rangle = (|\downarrow\uparrow\rangle - |\uparrow\downarrow\rangle)/\sqrt{2}$ [46,59]. Results in Figs. 3(c) and 3(d) reveal that the fidelity for $m = 0$ is 0.909 ± 0.024, while for $m = 4$, it is higher at

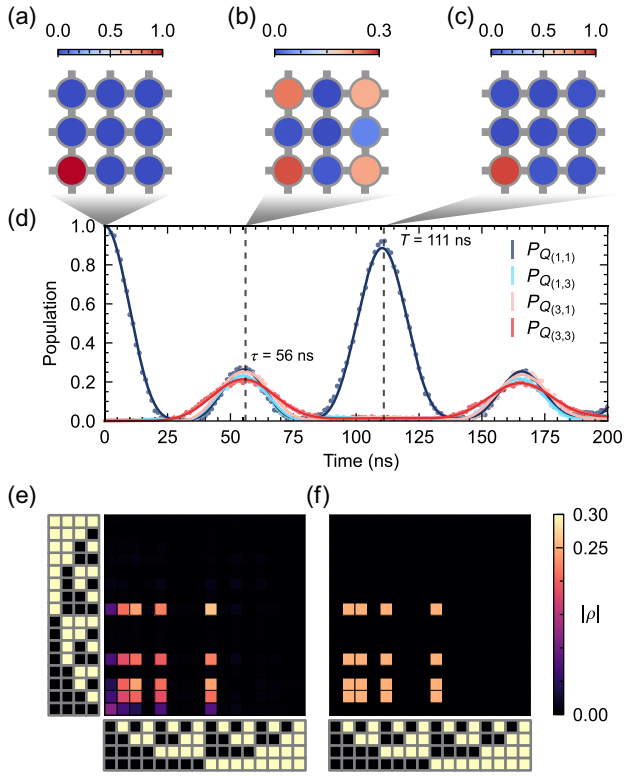


FIG. 4. Fractional state transfer and remote entanglement generation in a 2D (3×3) qubit network. (a)–(c) Population colormap of the 3×3 qubit network measured at $\tau = 0$, 56, and 111 ns, respectively. (d) The population measured at different times, with Q_1 initially prepared in a single-excitation state. For clarity, only the population of the four corner qubits is plotted. The symbols represent the experimental data, while the solid lines indicate the results from master equation simulations. (e) and (f) Experimentally reconstructed density matrix of the four corner qubits from the quantum state tomography (e) and its ideal form (f), yielding a state fidelity of 0.85. The left and bottom axes show matrix indices represented by binary strings, where black denotes the ground state $|\downarrow\rangle$ and light yellow denotes the excited state $|\uparrow\rangle$. The indices increase from $|\downarrow\downarrow\downarrow\downarrow\rangle$ to $|\uparrow\uparrow\uparrow\uparrow\rangle$ from left to right and bottom to top.

0.925 ± 0.021. All experiments with different m values are conducted on the same set of qubits within the same time period, demonstrating that increasing m can suppress decoherence, thereby enhancing the remote entanglement generation, which is essential for PST and FST in longer chains.

In Fig. 3(e), we further confirm the advantage of increasing m for noise suppression. To this end, we artificially introduce Gaussian-distributed noise to the frequencies of even qubits, i.e., let $\omega_n \to \omega_n + \xi_n$ ($n = 2, 4$), where $\xi_n \in N(0, \sigma)$ and σ denotes the noise intensity [46,73]. For each noisy frequency, we map it into an actual pulse amplitude using the single-qubit spectroscopy. The pulse duration is fixed to the FST operation time $\tau = 55.6$ ns. We then measure the fidelity degradation (i.e., F/F_0, where F_0 is the fidelity at zero noise) as a function of σ for different m. As the noise intensity increases from 0 to 30 MHz, the fidelity for $m = 0$ drops rapidly. In contrast, for $m = 4$ and $m = 6$, the fidelities degrade much more slowly. For instance, when $\sigma/2\pi = 30$ MHz, these values for $m = 0$, 4, and 6 are 0.56, 0.66, and 0.85, respectively. This is because as m increases, the even sites are much less occupied, and when m is large enough, the effective chain is reduced by half, as shown in Eqs. (10) and (11), which can significantly reduce the noise effect. For detailed experimental data and corresponding simulation results on the robustness of the zig-zag configuration against other types of noise, see Note 9 in the Supplemental Material [66].

V. EXTENSION TO TWO-DIMENSIONAL QUBIT NETWORK

Finally, we demonstrate the scalability of FST by extending the experiment to a 2D qubit network. This extension requires that the parameters $\omega_n^{x,y}$ and $J_n^{x,y}$ satisfy the FST conditions given by Eqs. (8), (9), and (13) along each respective dimension [42,46]. A detailed example of parameter construction is provided in Note 10 in the Supplemental Material [66]. To ensure experimental scalability, we developed a parameter calibration protocol that supports parallel execution, significantly reducing the total runtime, details of which are described in Note 7 in the Supplemental Material [66]. Figure 4(d) shows the population evolution of the four corner qubits by initially preparing an excitation on Q_1 at the lower-left corner, while Figs. 4(a)–4(c) display the population distribution of all 3×3 qubits at 0, 56, and 111 ns, respectively. At 56 ns, the excitation is uniformly transferred to the four corner qubits, suggesting that the system has evolved into a maximally entangled state between these qubits. By 111 ns, the system returns to the single-excitation state on Q_1, and this fractional revival process repeats periodically in subsequent evolution, providing experimental validation of the effectiveness of FST theory in the 2D case. We further perform quantum state tomography at 56 ns to reconstruct the density matrix ρ_{exp}, as shown in Fig. 4(e), while Fig. 4(f) shows the theoretical density matrix corresponding to the maximally entangled $\mathcal{W}$ state as [74]

$$|\mathcal{W}\rangle = \frac{1}{2}(|\uparrow\downarrow\downarrow\downarrow\rangle + |\downarrow\uparrow\downarrow\downarrow\rangle + |\downarrow\downarrow\uparrow\downarrow\rangle + |\downarrow\downarrow\downarrow\uparrow\rangle), \tag{14}$$

the experimentally reconstructed density matrix shows good agreement with the theoretical prediction, where the amplitudes are evenly distributed over the single-excitation indices with a value of 0.25. Decoherence effects introduce unexpected color blocks, thereby reducing the fidelity. The fidelity is defined as the overlap between the experimental and theoretical density matrices, measured as

$F = \mathrm{Tr}(\rho_{\mathrm{exp}} |\mathcal{W}\rangle\langle\mathcal{W}|) = 0.85$. To the best of our knowledge, this is the first experimental realization of a 2D $\mathcal{W}$ state based on the FST protocols. Simulations based on master equations for various m values in both 1D and 2D cases are presented in Note 10 in the Supplemental Material [66]. Finally, the total execution time for generating a generic $\mathcal{W}$ state on an $N \times N$ lattice, based on our scheme, is $\tau = \pi/J \approx \sqrt{1 + (4m/N)}\,(N\pi/4J_{\mathrm{max}})$, where J_{max} is the maximum coupling strength in the lattice. When $m \ll N$, which can be realized when N is sufficient large, $\tau \sim N\pi/(4J_{\mathrm{max}})$; and when $m \gg N$, $\tau \sim \sqrt{Nm}\pi/(2J_{\mathrm{max}})$. For this reason, the total execution time is not significantly increased for some appropriate values of m and N; see more details in Note 11 in the Supplemental Material [66].

VI. DISCUSSION AND CONCLUSION

To conclude, in this work, we propose a novel scheme for PST and FST based on a zig-zag configuration, enabling quantum state transfer and remote entanglement generation. Compared with the previous approach, this scheme offers a new degree of freedom—the energy difference between the even and odd sites, controlled by parameter m—which can effectively suppress the channel noise by reducing the occupation of the intermediate sites. A key feature of this model is that, when $m = 0$, it reduces to the conventional PST model with chain length N, and when $m \to \infty$, it reduces to the PST model with length $(N + 1)/2$ for odd N, revealing an elegant mathematical structure hidden in our newly designed model. Using this model, we demonstrate two key applications on systems with 3, 5, and 9 qubits. In the first application, we experimentally demonstrate PST and show that the energy difference associated with m can effectively integrate out the even sites, thereby suppressing noise. In the second application, we demonstrate remote entanglement generation via FST in both a 1D qubit chain and a 2D qubit network, generating a two-qubit Bell state and a four-qubit $\mathcal{W}$ state, respectively.

Our scheme can be generalized to larger quantum systems [46] and adapted to other quantum platforms, which have potential applications in quantum information processing and analog quantum simulation. In superconducting circuits, the primary limitation lies in the maximum achievable coupling strength between qubits. In the zig-zag configuration, the required maximum coupling appears near either J_1 or $J_{(N-1)/2}$, depending on the values of m and N as well as whether the goal is PST or FST. Regardless of its position, we find that the maximum coupling increases linearly with N, a trend that persists when extended to 2D architectures. For a fixed N, the maximum coupling increases with m following a square-root scaling. This implies that enhanced noise suppression via increasing m can be achieved without significantly compromising the required coupling strength, which is crucial for implementing state transfer and remote entanglement generation in future large-scale quantum processors [3,5,17,46]. Furthermore, an alternative model for PST and FST based on inverse design will be presented elsewhere [64]. These realizations are expected to play a key role in future quantum computers anticipated to scale to thousands of qubits, where quantum state transfer and remote entanglement generation are expected to become essential experimental techniques.

ACKNOWLEDGMENTS

This work is supported by the Strategic Priority Research Program of the Chinese Academy of Sciences (Grant No. XDB0500000), the National Natural Science Foundation of China (Grants No. 12034018 and No. U23A2074), and the Innovation Program for Quantum Science and Technology (No. 2021ZD0301200 and No. 2021ZD0301500). This work is also partially carried out at the USTC Center for Micro and Nanoscale Research and Fabrication.

DATA AVAILABILITY

The data that support the findings of this article are not publicly available. The data are available from the authors upon reasonable request.

[1] J. Preskill, Quantum computing in the NISQ era and beyond, Quantum **2**, 79 (2018).
[2] M. Brooks, Beyond quantum supremacy: The hunt for useful quantum computers, Nature **574**, 19 (2019).
[3] A. I. Google Quantum and Collaborators, Quantum error correction below the surface code threshold, Nature **638**, 920 (2025).
[4] F. Arute *et al.*, Quantum supremacy using a programmable superconducting processor, Nature **574**, 505 (2019).
[5] T. Jiang *et al.*, Generation of 95-qubit genuine entanglement and verification of symmetry-protected topological phases, arXiv:2505.01978.
[6] D. Gao *et al.*, Establishing a new benchmark in quantum computational advantage with 105-qubit Zuchongzhi 3.0 processor, Phys. Rev. Lett. **134**, 090601 (2025).
[7] Q. Zhu *et al.*, Quantum computational advantage via 60-qubit 24-cycle random circuit sampling, Sci. Bull. **67**, 240 (2022).
[8] Y. Wu *et al.*, Strong quantum computational advantage using a superconducting quantum processor, Phys. Rev. Lett. **127**, 180501 (2021).
[9] M. Gong *et al.*, Quantum walks on a programmable two-dimensional 62-qubit superconducting processor, Science **372**, 948 (2021).
[10] K. Wang *et al.*, Probing many-body bell correlation depth with superconducting qubits, Phys. Rev. X **15**, 021024 (2025).

[11] H. Dong *et al.*, Measuring the spectral form factor in many-body chaotic and localized phases of quantum processors, Phys. Rev. Lett. **134**, 010402 (2025).
[12] S. Xu *et al.*, Non-Abelian braiding of Fibonacci anyons with a superconducting processor, Nat. Phys. **20**, 1469 (2024).
[13] X. Zhang *et al.*, Digital quantum simulation of Floquet symmetry-protected topological phases, Nature **607**, 468 (2022).
[14] Z.-H. Liu *et al.*, Prethermalization by random multipolar driving on a 78-qubit superconducting processor, Nature **650**, 79 (2026).
[15] Y.-H. Shi *et al.*, Quantum simulation of topological zero modes on a 41-qubit superconducting processor, Phys. Rev. Lett. **131**, 080401 (2023).
[16] Y. Liu *et al.*, Interplay between disorder and topology in Thouless pumping on a superconducting quantum processor, Nat. Commun. **16**, 108 (2025).
[17] M. AbuGhanem, IBM quantum computers: Evolution, performance, and future directions, J. Supercomput. **81**, 687 (2025).
[18] Y. Kim, A. Eddins, S. Anand, K. X. Wei, E. van den Berg, S. Rosenblatt, H. Nayfeh, Y. Wu, M. Zaletel, K. Temme, and A. Kandala, Evidence for the utility of quantum computing before fault tolerance, Nature **618**, 500 (2023).
[19] E. J. Zhang *et al.*, High-performance superconducting quantum processors via laser annealing of transmon qubits, Sci. Adv. **8**, eabi6690 (2022).
[20] C.-L. Deng *et al.*, High-order topological pumping on a superconducting quantum processor, Phys. Rev. Lett. **133**, 140402 (2024).
[21] W. Huang *et al.*, Exact quantum critical states with a superconducting quantum processor, arXiv:2502.19185.
[22] J. Chu *et al.*, Scalable algorithm simplification using quantum AND logic, Nat. Phys. **19**, 126 (2023).
[23] H.-S. Zhong *et al.*, Phase-programmable Gaussian boson sampling using stimulated squeezed light, Phys. Rev. Lett. **127**, 180502 (2021).
[24] H.-S. Zhong *et al.*, Quantum computational advantage using photons, Science **370**, 1460 (2020).
[25] S. A. Moses *et al.*, A race-track trapped-ion quantum processor, Phys. Rev. X **13**, 041052 (2023).
[26] D. Bluvstein *et al.*, Logical quantum processor based on reconfigurable atom arrays, Nature **626**, 58 (2024).
[27] S. Storz, A. Kulikov, J. D. Schär, V. Barizien, X. Valcarce, F. Berterottière, N. Sangouard, J.-D. Bancal, and A. Wallraff, Complete self-testing of a system of remote superconducting qubits, Phys. Rev. Lett. **135**, 030801 (2025).
[28] S. Storz *et al.*, Loophole-free bell inequality violation with superconducting circuits, Nature **617**, 265 (2023).
[29] P. Magnard, S. Storz, P. Kurpiers, J. Schar, F. Marxer, J. Lutolf, T. Walter, J. C. Besse, M. Gabureac, K. Reuer, A. Akin, B. Royer, A. Blais, and A. Wallraff, Microwave quantum link between superconducting circuits housed in spatially separated cryogenic systems, Phys. Rev. Lett. **125**, 260502 (2020).
[30] J. Song, S. Yang, P. Liu, H.-L. Zhang, G.-M. Xue, Z.-Y. Mi, W.-G. Zhang, F. Yan, Y.-R. Jin, and H.-F. Yu, Realization of high-fidelity perfect entangler between remote superconducting quantum processors, arXiv:2407.20338.
[31] X. Deng, W. Zheng, X. Liao, H. Zhou, Y. Ge, J. Zhao, D. Lan, X. Tan, Y. Zhang, S. Li, and Y. Yu, Long-range *ZZ* interaction via resonator-induced phase in superconducting qubits, Phys. Rev. Lett. **134**, 020801 (2025).
[32] M. Mollenhauer, A. Irfan, X. Cao, S. Mandal, and W. Pfaff, A high-efficiency plug-and-play superconducting qubit network, arXiv:2407.16743 (2024).
[33] J. Niu *et al.*, Demonstrating path-independent anyonic braiding on a modular superconducting quantum processor, Phys. Rev. Lett. **132**, 20601 (2024).
[34] J. Qiu, Y. Liu, L. Hu, Y. Wu, J. Niu, L. Zhang, W. Huang, Y. Chen, J. Li, S. Liu, Y. Zhong, L. Duan, and D. Yu, Deterministic quantum state and gate teleportation between distant superconducting chips, Sci. Bull. (Beijing) **70**, 351 (2025).
[35] J. Niu *et al.*, Low-loss interconnects for modular superconducting quantum processors, Nat. Electron. **6**, 235 (2023).
[36] Y. Zhong, H. S. Chang, A. Bienfait, E. Dumur, M. H. Chou, C. R. Conner, J. Grebel, R. G. Povey, H. Yan, D. I. Schuster, and A. N. Cleland, Deterministic multi-qubit entanglement in a quantum network, Nature **590**, 571 (2021).
[37] A. Gold, J. P. Paquette, A. Stockklauser, M. J. Reagor, M. S. Alam, A. Bestwick, N. Didier, A. Nersisyan, F. Oruc, A. Razavi, B. Scharmann, E. A. Sete, B. Sur, D. Venturelli, C. J. Winkleblack, F. Wudarski, M. Harburn, and C. Rigetti, Entanglement across separate silicon dies in a modular superconducting qubit device, npj Quantum Inf. **7**, 142 (2021).
[38] K. N. Smith, G. S. Ravi, J. M. Baker, and F. T. Chong, in *2022 55th IEEE/ACM International Symposium on Microarchitecture (MICRO)* (IEEE, Chicago, IL, USA, 2022), pp. 1092–1109.
[39] M. Malekakhlagh, T. Phung, D. Puzzuoli, K. Heya, N. Sundaresan, and J. Orcutt, Enhanced quantum state transfer and Bell-state generation over long-range multimode interconnects via superadiabatic transitionless driving, Phys. Rev. Appl. **22**, 024006 (2024).
[40] M. Christandl, N. Datta, A. Ekert, and A. J. Landahl, Perfect state transfer in quantum spin networks, Phys. Rev. Lett. **92**, 187902 (2004).
[41] M.-H. Yung and S. Bose, Perfect state transfer, effective gates, and entanglement generation in engineered bosonic and fermionic networks, Phys. Rev. A **71**, 032310 (2005).
[42] A. Kay, Perfect, efficient, state transfer and its application as a constructive tool, Int. J. Quantum Inf. **08**, 641 (2010).
[43] V. X. Genest, L. Vinet, and A. Zhedanov, Quantum spin chains with fractional revival, Ann. Phys. (N.Y.) **371**, 348 (2016).
[44] X. Li, Y. Ma, J. Han, T. Chen, Y. Xu, W. Cai, H. Wang, Y. P. Song, Z.-Y. Xue, Z.-Q. Yin, and L. Sun, Perfect quantum state transfer in a superconducting qubit chain with parametrically tunable couplings, Phys. Rev. Appl. **10**, 054009 (2018).
[45] C. Zhang, T.-L. Wang, Z.-A. Zhao, X.-Y. Yang, L.-L. Guo, Z.-L. Jia, P. Duan, and G.-P. Guo, Fast and perfect state transfer in superconducting circuit with tunable coupler, Chin. Phys. B **32**, 110305 (2023).

[46] L. Xiang, J. Chen, Z. Zhu, Z. Song, Z. Bao, X. Zhu, F. Jin, K. Wang, S. Xu, Y. Zou, H. Li, Z. Wang, C. Song, A. Yue, J. Partridge, Q. Guo, R. Mondaini, H. Wang, and R. T. Scalettar, Enhanced quantum state transfer by circumventing quantum chaotic behavior, Nat. Commun. **15**, 4918 (2024).

[47] F. A. Roy *et al.*, Parity-dependent state transfer for direct entanglement generation, Nat. Commun. **16**, 2660 (2025).

[48] R. J. Chapman, M. Santandrea, Z. Huang, G. Corrielli, A. Crespi, M. H. Yung, R. Osellame, and A. Peruzzo, Experimental perfect state transfer of an entangled photonic qubit, Nat. Commun. **7**, 11339 (2016).

[49] A. Perez-Leija, R. Keil, A. Kay, H. Moya-Cessa, S. Nolte, L.-C. Kwek, B. M. Rodríguez-Lara, A. Szameit, and D. N. Christodoulides, Coherent quantum transport in photonic lattices, Phys. Rev. A **87**, 012309 (2013).

[50] M. Bellec, G. M. Nikolopoulos, and S. Tzortzakis, Faithful communication Hamiltonian in photonic lattices, Opt. Lett. **37**, 4504 (2012).

[51] J. Zhang, G. L. Long, W. Zhang, Z. Deng, W. Liu, and Z. Lu, Simulation of Heisenberg *XY* interactions and realization of a perfect state transfer in spin chains using liquid nuclear magnetic resonance, Phys. Rev. A **72**, 012331 (2005).

[52] T. Tian, S. Lin, L. Zhang, P. Yin, P. Huang, C. Duan, L. Jiang, and J. Du, Perfect coherent transfer in an on-chip reconfigurable nanoelectromechanical network, Phys. Rev. B **101**, 174303 (2020).

[53] P. Kurpiers, P. Magnard, T. Walter, B. Royer, M. Pechal, J. Heinsoo, Y. Salathe, A. Akin, S. Storz, J. C. Besse, S. Gasparinetti, A. Blais, and A. Wallraff, Deterministic quantum state transfer and remote entanglement using microwave photons, Nature **558**, 264 (2018).

[54] C. J. Axline, L. D. Burkhart, W. Pfaff, M. Zhang, K. Chou, P. Campagne-Ibarcq, P. Reinhold, L. Frunzio, S. M. Girvin, L. Jiang, M. H. Devoret, and R. J. Schoelkopf, On-demand quantum state transfer and entanglement between remote microwave cavity memories, Nat. Phys. **14**, 705 (2018).

[55] P. Campagne-Ibarcq, E. Zalys-Geller, A. Narla, S. Shankar, P. Reinhold, L. Burkhart, C. Axline, W. Pfaff, L. Frunzio, R. J. Schoelkopf, and M. H. Devoret, Deterministic remote entanglement of superconducting circuits through microwave two-photon transitions, Phys. Rev. Lett. **120**, 200501 (2018).

[56] Y. P. Zhong, H. S. Chang, K. J. Satzinger, M. H. Chou, A. Bienfait, C. R. Conner, É. Dumur, J. Grebel, G. A. Peairs, R. G. Povey, D. I. Schuster, and A. N. Cleland, Violating bell's inequality with remotely connected superconducting qubits, Nat. Phys. **15**, 741 (2019).

[57] A. Bienfait, K. J. Satzinger, Y. P. Zhong, H. S. Chang, M. H. Chou, C. R. Conner, É. Dumur, J. Grebel, G. A. Peairs, R. G. Povey, and A. N. Cleland, Phonon-mediated quantum state transfer and remote qubit entanglement, Science **364**, 368 (2019).

[58] N. Leung, Y. Lu, S. Chakram, R. K. Naik, N. Earnest, R. Ma, K. Jacobs, A. N. Cleland, and D. I. Schuster, Deterministic bidirectional communication and remote entanglement generation between superconducting qubits, npj Quantum Inf. **5**, 18 (2019).

[59] H. S. Chang, Y. P. Zhong, A. Bienfait, M. H. Chou, C. R. Conner, E. Dumur, J. Grebel, G. A. Peairs, R. G. Povey, K. J. Satzinger, and A. N. Cleland, Remote entanglement via adiabatic passage using a tunably dissipative quantum communication system, Phys. Rev. Lett. **124**, 240502 (2020).

[60] F. Yan, P. Krantz, Y. Sung, M. Kjaergaard, D. L. Campbell, T. P. Orlando, S. Gustavsson, and W. D. Oliver, Tunable coupling scheme for implementing high-fidelity two-qubit gates, Phys. Rev. Appl. **10**, 054062 (2018).

[61] C. Zhang, T.-L. Wang, L.-L. Guo, X.-Y. Yang, X.-X. Yang, P. Duan, Z.-L. Jia, W.-C. Kong, and G.-P. Guo, Characterization of tunable coupler without a dedicated readout resonator in superconducting circuits, Appl. Phys. Lett. **122**, 024001 (2023).

[62] G. M. L. Gladwell, *Inverse Problems in Vibration*, Solid Mechanics and Its Applications Vol. 119 (Springer Science & Business Media, 2005).

[63] M. Chu and G. Golub, *Inverse Eigenvalue Problems: Theory, Algorithms, and Applications* (Oxford University Press, 2005).

[64] T.-L. Wang, Z.-A. Zhao, P. Wang *et al.*, Inverse designed Hamiltonian for perfect state transfer and remote entanglement generation, and applications in superconducting qubits, (to be published).

[65] H.-T. Hu, X. Lin, A.-M. Guo, Z. Lin, and M. Gong, Hidden self-duality in quasiperiodic network models, Phys. Rev. Lett. **134**, 246301 (2025).

[66] See Supplemental Material at http://link.aps.org/supplemental/10.1103/4x8d-cmyx for details, which includes Refs. [75–93].

[67] X.-Y. Yang, H.-F. Zhang, L. Du, H.-R. Tao, L.-L. Guo, T.-L. Wang, Z.-L. Jia, W.-C. Kong, Z.-Y. Chen, P. Duan, and G.-P. Guo, Fast, universal scheme for calibrating microwave crosstalk in superconducting circuits, Appl. Phys. Lett. **125**, 044001 (2024).

[68] J. X. Zhang, Z.-Y. Chen, Y.-J. Wang, B.-H. Lu, H.-F. Zhang, J.-N. Li, P. Duan, Y.-C. Wu, and G.-P. Guo, Demonstrating a universal logical gate set in error-detecting surface codes on a superconducting quantum processor, arXiv:2405.09035.

[69] S. Zhang *et al.*, Demonstrating coherent quantum routers for bucket-brigade quantum random access memory on a superconducting processor, arXiv:2505.13958.

[70] H.-F. Zhang *et al.*, Experimental robustness benchmark of quantum neural network on a superconducting quantum processor, arXiv:2505.16714.

[71] P. Wang, B.-H. Lu, T.-L. Wang, S. Zhang, Z.-Y. Chen, H.-F. Zhang, R.-Z. Zhao, X.-Y. Yang, Z.-A. Zhao, Z.-Z. Zhang, X.-X. Song, Y.-C. Wu, P. Duan, and G.-P. Guo, Spectator leakage elimination in CZ gates via tunable coupler interference on a superconducting quantum processor, arXiv:2507.14531.

[72] J. A. Smolin, J. M. Gambetta, and G. Smith, Efficient method for computing the maximum-likelihood quantum state from measurements with additive Gaussian noise, Phys. Rev. Lett. **108**, 070502 (2012).

[73] F. Mei, G. Chen, L. Tian, S.-L. Zhu, and S. Jia, Robust quantum state transfer via topological edge states in superconducting qubit chains, Phys. Rev. A **98**, 012331 (2018).

[74] M. Neeley, R. C. Bialczak, M. Lenander, E. Lucero, M. Mariantoni, A. D. O'Connell, D. Sank, H. Wang, M. Weides, J. Wenner, Y. Yin, T. Yamamoto, A. N. Cleland, and J. M. Martinis, Generation of three-qubit entangled states using superconducting phase qubits, Nature **467**, 570 (2010).

[75] P. V. Klimov, J. Kelly, J. M. Martinis, and H. Neven, The snake optimizer for learning quantum processor control parameters, arXiv:2006.04594.

[76] P. Duan, Z. Jia, C. Zhang, L. Du, H. Tao, X. Yang, L. Guo, Y. Chen, H. Zhang, Z. Peng, W. Kong, H.-O. Li, G. Cao, and G.-P. Guo, Broadband flux-pumped Josephson parametric amplifier with an on-chip coplanar waveguide impedance transformer, Appl. Phys. Express **14**, 042011 (2021).

[77] Y.-Y. Wang *et al.*, Exploring Hilbert-space fragmentation on a superconducting processor, PRX Quantum **6**, 010325 (2025).

[78] H. Li, Y.-Y. Wang, Y.-H. Shi, K. Huang, X. Song, G.-H. Liang, Z.-Y. Mei, B. Zhou, H. Zhang, J.-C. Zhang, S. Chen, S. P. Zhao, Y. Tian, Z.-Y. Yang, Z. Xiang, K. Xu, D. Zheng, and H. Fan, Observation of critical phase transition in a generalized Aubry-André-Harper model with superconducting circuits, npj Quantum Inf. **9**, 40 (2023).

[79] Z.-C. Xiang, K. Huang, Y.-R. Zhang, T. Liu, Y.-H. Shi, C.-L. Deng, T. Liu, H. Li, G.-H. Liang, Z.-Y. Mei, H. Yu, G. Xue, Y. Tian, X. Song, Z.-B. Liu, K. Xu, D. Zheng, F. Nori, and H. Fan, Simulating Chern insulators on a superconducting quantum processor, Nat. Commun. **14**, 5433 (2023).

[80] P. Virtanen *et al.* (SciPy 1.0 Contributors), SciPy 1.0: Fundamental algorithms for scientific computing in Python, Nat. Methods **17**, 261 (2020).

[81] J. Jazzbin, "Geatpy: The genetic and evolutionary algorithm toolbox with high performance in python", https://github.com/geatpy-dev/geatpy/ (accessed 2020) (2020).

[82] A. Javadi-Abhari, M. Treinish, K. Krsulich, C. J. Wood, J. Lishman, J. Gacon, S. Martiel, P. D. Nation, L. S. Bishop, A. W. Cross, B. R. Johnson, and J. M. Gambetta, Quantum computing with Qiskit, arXiv:2405.08810.

[83] S. Diamond and S. Boyd, CVXPY: A Python-embedded modeling language for convex optimization, J. Mach. Learn. Res. **17**, 2909 (2016).

[84] A. Agrawal, R. Verschueren, S. Diamond, and S. Boyd, A rewriting system for convex optimization problems, J. Control Decis. **5**, 42 (2018).

[85] G. C. Knee, E. Bolduc, J. Leach, and E. M. Gauger, Quantum process tomography via completely positive and trace-preserving projection, Phys. Rev. A **98**, 062336 (2018).

[86] S. T. Merkel, J. M. Gambetta, J. A. Smolin, S. Poletto, A. D. Córcoles, B. R. Johnson, C. A. Ryan, and M. Steffen, Self-consistent quantum process tomography, Phys. Rev. A **87**, 062119 (2013).

[87] A. N. Korotkov, Error matrices in quantum process tomography, arXiv:1309.6405.

[88] J. Johansson, P. Nation, and F. Nori, QuTiP: An open-source Python framework for the dynamics of open quantum systems, Comput. Phys. Commun. **183**, 1760 (2012).

[89] J. Johansson, P. Nation, and F. Nori, QuTiP 2: A Python framework for the dynamics of open quantum systems, Comput. Phys. Commun. **184**, 1234 (2013).

[90] A. Blais, A. L. Grimsmo, S. M. Girvin, and A. Wallraff, Circuit quantum electrodynamics, Rev. Mod. Phys. **93**, 025005 (2021).

[91] L.-L. Guo, P. Duan, S. Zhang, X.-X. Yang, C. Zhang, L. Du, H.-F. Zhang, H.-R. Tao, T.-L. Wang, Z.-L. Jia, Z.-Y. Chen, and G.-P. Guo, Universal scalable characterization and correction of pulse distortions in controlled quantum systems, Phys. Rev. Appl. **21**, 064060 (2024).

[92] L. E. Fischer, A. Chiesa, F. Tacchino, D. J. Egger, S. Carretta, and I. Tavernelli, Universal qudit gate synthesis for transmons, PRX Quantum **4**, 030327 (2023).

[93] J.-M. Cai, Z.-W. Zhou, and G.-C. Guo, Decoherence effects on the quantum spin channels, Phys. Rev. A **74**, 022328 (2006).